processes

MDPI

Article

Effect of Support on Steam Reforming of Ethanol for H_2 Production with Copper-Based Catalysts

Ramiro Picoli Nippes [1], Paula Derksen Macruz [2], Aline Domingues Gomes [2], Marcos de Souza [2], Bruna Rodrigues Ferreira [3], Roberta Carolina Pelissari Rizzo-Domingues [3] and Luiz Pereira Ramos [1,*]

[1] Graduate Program in Chemical Engineering, Federal University of Parana, R. Francisco H. dos Santos, Curitiba 81531-990, Paraná, Brazil; ramiro_picoli@yahoo.com.br
[2] Department of Chemical Engineering, Maringa State University, Av. Colombo, 5790, Maringá 87020-900, Paraná, Brazil; pauladmacruz@gmail.com (P.D.M.); alinedgs@gmail.com (A.D.G.); msouza2@uem.br (M.d.S.)
[3] Department of Chemical and Biology, Federal Technology University of Paraná, Av. Heitor de Alencar Furtado, 5000, Curitiba 81280-340, Paraná, Brazil; bruna1.ferreira@yahoo.com.br (B.R.F.); robertac@utfpr.edu.br (R.C.P.R.-D.)
* Correspondence: luiz.ramos@ufpr.br; Tel.: +55-(41)-99963-6084

Abstract: Catalytic studies hydrogen production via steam reforming of ethanol (SRE) are essential for process optimization. Likewise, selecting the ideal support for the active phase can be critical to achieve high conversion rates during the catalytic steam reforming process. In this work, copper-based catalysts were synthesized using two different supports, NaY zeolite and Nb_2O_5/Al_2O_3 mixed oxides. The materials were prepared using wet impregnation and characterized for their physico-chemical properties using different analytical techniques. Differences in the catalyst morphologies were readily attributed to the characteristics of the support. The Cu/NaY catalyst exhibited a higher specific surface area (210.40 $m^2\ g^{-1}$) compared to the $Cu/Nb_2O_5/Al_2O_3$ catalyst (26.00 $m^2\ g^{-1}$), resulting in a homogeneous metal dispersion over the support surface. The obtained results showed that, at 300 °C, both the $Cu/Nb_2O_5/Al_2O_3$ and Cu/NaY catalysts produced approximately 50% hydrogen and 40% acetaldehyde, but with significant differences in conversion (6% and 56%, respectively). At 450 °C, a greater product distribution and a 10% higher conversion were observed when the catalyst was supported on NaY compared to Nb_2O_5/Al_2O_3. Hence, the performance of copper-based catalysts was influenced significantly by the textural properties of the support.

Keywords: ethanol steam reforming; hydrogen production; copper-based catalysts; zeolite; mixed oxides

Citation: Nippes, R.P.; Macruz, P.D.; Domingues Gomes, A.; de Souza, M.; Ferreira, B.R.; Rizzo-Domingues, R.C.P.; Pereira Ramos, L. Effect of Support on Steam Reforming of Ethanol for H_2 Production with Copper-Based Catalysts. *Processes* **2024**, *12*, 1331. https://doi.org/10.3390/pr12071331

Academic Editor: Limo He

Received: 29 May 2024
Revised: 20 June 2024
Accepted: 23 June 2024
Published: 27 June 2024

1. Introduction

The increasing global demand for energy, coupled with the socioenvironmental impacts of an energy matrix that is still heavily reliant on traditional fossil fuels such as coal, crude oil, and natural gas [1,2], requires the development of sustainable production processes to support the transition to a new and more diversified energy matrix. Among the sustainable alternatives for this energy transition, hydrogen (H_2) stands out as one of the most prominent.

H_2 can be obtained through different pathways such as electrolysis [3,4], biological reactions [5], biomass gasification [6], steam reforming [7,8], aqueous phase reforming [9], and partial oxidation of hydrocarbons and alcohols [10]. Among these possibilities, the use of ethanol as feedstock for H_2 production in fuel cells has considerable advantages. These include easier storage, handling, and safe transportation due to its low toxicity and volatility. Additionally, ethanol is a renewable feedstock when obtained through biomass fermentation, is rich in H_2, and has a nearly closed carbon cycle that helps in the abatement of greenhouse gas emissions [11,12]. Thus, the steam reforming of ethanol (SRE) emerges

as an attractive solution for H_2 production due to its high H_2 yield and thermodynamic feasibility [13].

SRE for H_2 production is a catalytic process. Therefore, H_2 yield depends on the properties of the catalyst to be employed [14]. This includes the catalytic support for the active phase [15] and the method used for catalyst preparation [16]. In general, the catalyst design is crucial for a successful SRE process. Different catalytic systems have been investigated for SRE using noble and non-noble metal-based catalysts [17]. Among them, copper-based catalysts [18–20] have the advantage of being cost-effective and widely available compared to other metals. Copper as an active phase is widely used in commercial catalysts for methanol reforming. Additionally, the presence of copper active sites promotes ethanol steam reforming to produce H_2 and CO or its dehydrogenation to acetaldehyde followed by decarbonylation, producing CH_4 and CO [21–23]. Hence, copper-based catalysts have potential for SRE applications.

The choice of support for the active phase is extremely important for SRE because it plays a significant role in H_2 selectivity and catalyst stability [24,25], as already demonstrated in previous studies [26,27]. In general, efficient SRE supports must have favorable textural properties and moderate acidity, in addition to being relatively cheap, readily available, and easily accessible. In this study, two supports were selected and evaluated for their effect on H_2 production by SRE using copper as the catalytic active phase.

The first selected support was NaY, a commercially available zeolite that is known for its high heat resistance, unique ordered three-dimensional porous structure, and larger pores compared to the dimensions of the ethanol molecule, as well as low production costs [28,29]. For instance, NaY can be synthesized from alternative, abundant, and inexpensive materials such as rice husks [30,31] and wheat straw [32] ashes. Several studies have already demonstrated the application of NaY as a catalyst support for SRE [33–35]. The other selected support was a Nb_2O_5/Al_2O_3 mixed oxide. Alumina is widely used as a support in heterogeneous catalysis [36–40] due to its large surface area, good stability, and wide commercial availability [41]. Nb_2O_5 is also a notable material in the field of catalysis, known for its non-toxic nature, suitable acid properties [42,43], excellent chemical stability, high thermodynamic stability, low cost, and high commercial availability [44,45]. The combination of Nb_2O_5 with alumina is favorable because, being an n-type semiconductor, Nb_2O_5 can interact with copper in catalytic active reaction sites [46,47]. Additionally, Nb_2O_5 is structurally similar to commercial catalysts for methanol reforming ($Cu/ZnO/Al_2O_3$). Since ZnO is also an n-type semiconductor oxide, Nb_2O_5 may have similar catalytic properties.

This study aimed at evaluating the effect of NaY and Nb_2O_5/Al_2O_3 as the catalyst support for SRE. H_2 production was carried out using copper as the active phase under the same reaction conditions. To the best of our knowledge, these supports have never been compared in SRE reactions with copper used as the active phase. Copper was anchored on the support surface by wet impregnation. Then, the resulting catalytic systems were characterized using various analytical techniques and subjected to SRE using an experimental reaction module.

2. Materials and Methods

2.1. Material

Materials were synthesized using copper nitrate ($Cu(NO_3)2{\cdot}3H_2O$, 98%) from Sigma-Aldrich, commercial alumina (Al_2O_3, 90%) from Merck, NaY zeolite from Sigma-Aldrich, and niobic acid (HY-340) from the Brazilian Metallurgy and Mining Company (CBMM). HY-340 was heat-treated to obtain niobium pentoxide (Nb_2O_5).

2.2. Methods

2.2.1. Catalyst Preparation

The catalysts were prepared using a simple wet impregnation methodology under solvent excess [48]. For the Cu/NaY catalyst, 57.25 g $Cu(NO_3)_2{\cdot}3H_2O$ were dissolved in

water and mixed with 14.94 g of the NaY support. For the $Cu/Nb_2O_5/Al_2O_3$ catalyst, 57.25 g $Cu(NO_3)_2{\cdot}3H_2O$ were dissolved in water and mixed with 9.27 g Nb_2O_5 and 5.67 g Al_2O_3. The mixtures were placed in a rotary evaporator and evaporated for 2 h at 343 K for the complete elimination of water. After this, the materials were placed in an oven at 353 K for about 10 h. Then, the dried materials were crushed and placed in a muffle furnace in ambient atmosphere. The temperature was raised to 773.15 K using a 10 K min^{-1} heating rate, and the catalysts remained at this plateau for 5 h. At the end of the process, two catalysts, named Cu/NaY and Cu/ $Nb_2O_5/Al_2O_{3,}$ were obtained.

2.2.2. Catalyst Characterization

Scanning Electron Microscopy (SEM) was performed using a Zeiss EVO MA15 microscope coupled with an X-Max 20 mm^2 Energy Dispersive Spectrometer (EDS). X-ray Diffraction (XRD) analyses were conducted on a Shimadzu XDR-7000 diffractometer using CuKα radiation. Measurements were taken at 40 kV and 30 mA using a Cu tube with a wavelength of 1.54 nm, with a scan rate of 2° min^{-1} and an interval of $5° \leq 2\theta \leq 80°$. The FWHM of the XRD peaks was used to estimate the average particle size using the Scherrer equation (Equation (1)).

$$D_{(hkl)} = \frac{0.9 \times \lambda}{\beta_{(hkl)} \times \theta}, \quad (1)$$

The textural properties of the catalysts were determined by N_2 adsorption/desorption at 77 K using a NOVA-4000-Quantachrome adsorption analyzer. Infrared spectroscopy analyses (FTIR) were performed using a Varian 640-IR spectrometer with potassium bromide (KBr) as the dispersing agent in the region from 4000 to 400 cm^{-1}. Temperature-programmed desorption of NH_3 (TPD-NH_3) and temperature-programmed reduction (TPR) were carried out using a Quantachrome Chembet-3000 multi-use unit coupled with a ThermoStar-GSD 301 mass spectrometer. In both analyses, 0.1 g sample was placed in a "U"-shaped quartz reactor, which was first subjected to a 20 cm^3 min^{-1} N_2 flow at 300 °C for 1 h to remove humidity and possibly adsorbed materials. For TPD-NH_3 analysis, the samples were reduced with 1.75% H_2 diluted in N2 for 1 h using a heating rate of 10 °C min^{-1} from room temperature to 500 °C and remaining at this temperature for another 1 h. NH_3 adsorption was performed at 100 °C for 30 min with a flow rate of 15 cm^3 min^{-1} of 5% NH_3 diluted in N_2. Subsequently, the system was purged for 2 h with a flow rate of 20 cm^3 min^{-1} N2. Finally, the sample was heated to 700 °C at a heating rate of 10 °C min^{-1} under N2 flow for NH_3 desorption. TPR was performed with a reducing gas feed containing 1.75% H_2 in N2 at a flow rate of 20 cm^3 min^{-1}, progressing from room temperature to 1000 °C with a heating rate of 10 °C min^{-1}.

2.2.3. Catalytic Performance Evaluation

SRE was carried out using two catalysts, Cu/NaY and $Cu/Nb_2O_5/Al_2O_3$. Tests were performed in an experimental unit consisting of a preheating system, a 20 cm-long stainless-steel reactor with an internal diameter of 2.54 cm, a condenser, and a phase collector/separator. The reactant mixture was introduced through the system inlet using a peristaltic pump.

Before the catalytic tests, the catalysts were activated in situ with an 85 cm^3 min^{-1} N_2 flow rate containing 40% H_2 by volume using the following heating steps: 30 min at 100 °C, 1 h at 200 °C, and 4 h at 500 °C. After this, the H_2 flow was stopped, and the N_2 flow was adjusted to 85 mL min^{-1} for 4 h to purge H_2 from the entire reaction system. Subsequently, catalytic tests were conducted at 300 °C and 450 °C using a mass hourly space velocity of 40 dm^3 h^{-1} $g_{cat}{}^{-1}$, 5 g catalyst (20–40 mesh, positioned at the center with the reactor ends filled with silica of the same particle size), and a H_2O/C_2H_5OH molar ratio of 10/1 without the presence of an inert. The pellet size distribution was determined according to Trimm [49] to minimize both mass and heat diffusion effects in packed bed

reactors ($L/d_{part} \geq 100$ and $D/d_{part} \geq 30$), resulting in a mean particle size distribution of 0.6 mm. The carbon balance was determined as described in Equation (2),

$$C(\%) = \left(\frac{\sum_i F_i nc_i}{F_{in}^{EtOH} nc_i} \right) \times 100 \quad (2)$$

where F_i is the molar flow rate of carbon in the products, nc_i is the corresponding number of carbons, and F_{in}^{EtOH} is the molar flow rate at the inlet.

The gaseous products were analyzed in a Trace GC ThermoQuest gas chromatograph with a Carboxen 1010 PLOT column, with argon as carrier gas, detection by TCD, and the following temperature program: 7 min at 45 °C, 25 °C min^{-1} to 180 °C, and 5 min at 180 °C. The liquid phase was analyzed in a Varian 3300 gas chromatograph using a 10% Carbowax 20M CHR W HP column, helium as carrier gas, detection by TCD, and the following temperature program: 2 min at 50 °C, 25 °C min^{-1} to 100 °C, and 2 min at 100 °C.

Evaluation of catalytic performance for H_2 production was based on ethanol conversion (C_{EtOH}) and product selectivity (S_i) on dry basis following Equations (3) and (4),

$$C_{EtOH}(\%) = \left(\frac{F_{in}^{EtOH} - F_{out}^{EtOH}}{F_{in}^{EtOH}} \right) \times 100 \quad (3)$$

$$S_i(\%) = \left(\frac{F_i}{\sum F_i} \right) \times 100 \quad (4)$$

where F_{in}^{EtOH} is the molar flow rate of ethanol at the inlet, F_{out}^{EtOH} is the molar flow rate of ethanol at the outlet, and F_i is the molar flow rate of i-species.

3. Results and Discussion

3.1. Catalyst Characterization

3.1.1. Morphology

SEM was used to analyze the microstructural morphology of the catalysts. Figure 1a shows the NaY support, and Figure 1b shows the synthesized Cu/NaY catalyst. Even after the wet impregnation of copper on the NaY support, the polyhedral shapes of the zeolite remained regular and homogeneous, indicating no change in its morphological structure. By contrast, Figure 1c shows the Nb_2O_5 support, while Figure 1d shows the synthesized $Cu/Nb_2O_5/Al_2O_3$ catalyst. Unlike Cu/NaY, the particles are randomly distributed with various geometries and distinct sizes. These morphological properties were attributed to the nature of the support used, which does not present a well-defined microstructural morphology and evenly distributed particle sizes.

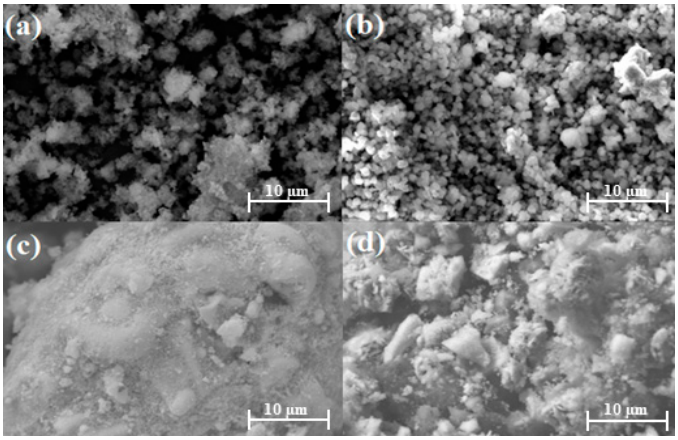

Figure 1. SEM at 4000× of (**a**) NaY, (**b**) Cu/NaY, (**c**) Nb_2O_5, and (**d**) $Cu/Nb_2O_5/Al_2O_3$.

Elemental mapping was performed by EDS to identify chemical elements at the catalyst surface using a magnification of 4000×. Figure 2 shows that all proposed elements were detected, indicating the effectiveness of the proposed wet impregnation process. Additionally, Cu seemed to be better dispersed on NaY compared to Nb_2O_5/Al_2O_3, which presented higher Cu concentrations in some regions. This is strongly linked to the superior textural properties of the zeolite, which allowed for a better distribution of the metal particles.

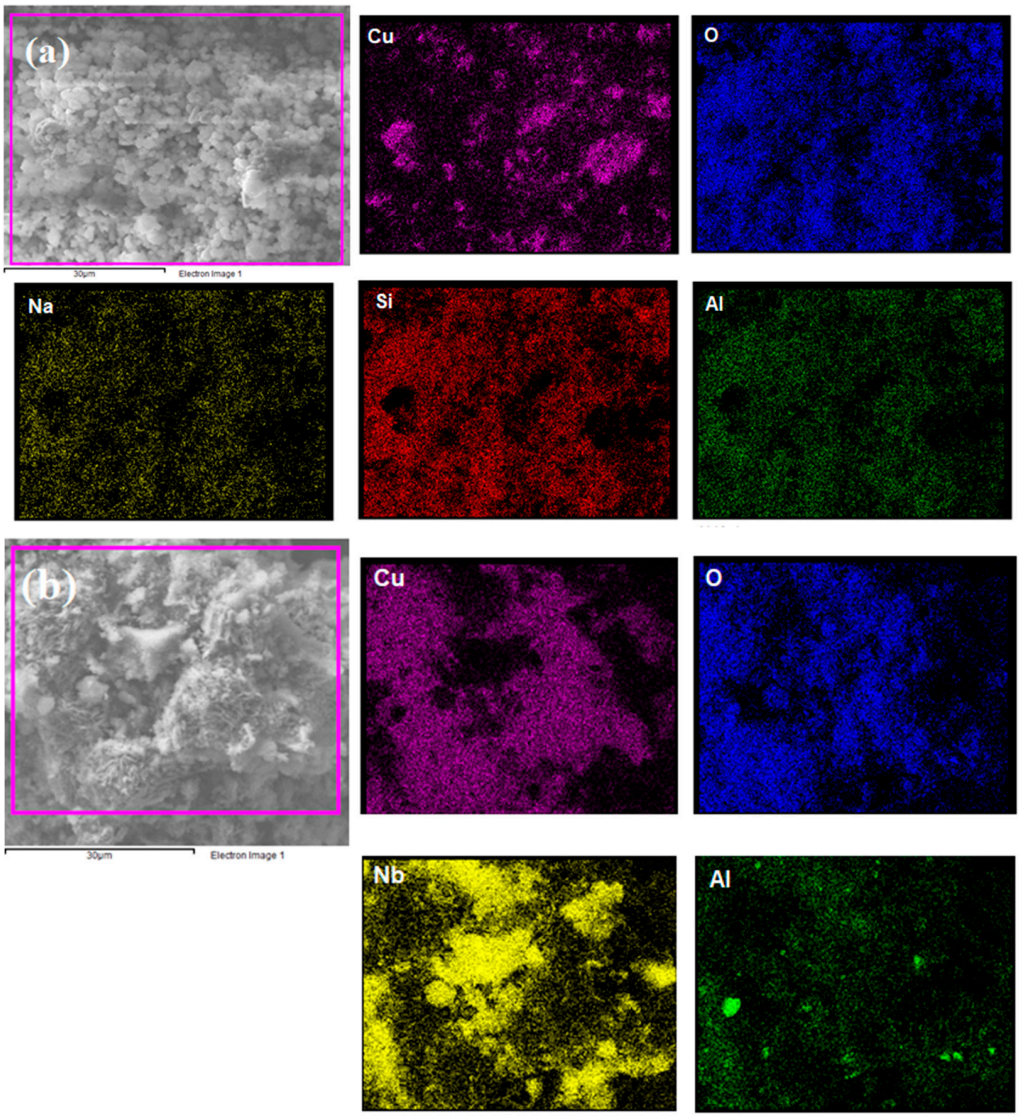

Figure 2. Elemental mapping of (**a**) Cu/NaY and (**b**) $Cu/Nb_2O_5/Al_2O_3$.

Table 1 presents the EDS mass composition of the catalysts. Cu was present in both catalysts in very similar percentages. Furthermore, a Si/Al ratio of 2.58 confirmed the presence of an unmodified NaY zeolite after the wet impregnation synthesis.

Table 1. Elemental analysis of Cu/NaY and $Cu/Nb_2O_5/Al_2O_3$.

Sample	Element (%)						
	Cu	**Na**	**Al**	**Si**	**O**	**Nb**	**C**
Cu/NAY	11.90	3.87	3.00	7.76	26.75	-	3.01
$Cu/Nb_2O_5/Al_2O_3$	11.17	-	2.84	-	15.72	10.82	0.88

3.1.2. Crystallinity

The XRD technique was employed to determine the crystallinity and purity of the synthesized catalysts. The experimental XRD patterns obtained for Cu/NaY and $Cu/Nb_2O_5/Al_2O_3$ are shown in Figure 3. For the Cu/NaY catalyst, the diffraction peaks at 2θ = 6.18°, 15.61°, 18.66°, 23.64°, 26.98°, and 31.36° are indexed to the cubic crystal structure of NaY, which corresponds to the Fd-3m space group in card #00-039-1380. The diffraction peaks at 2θ = 35.57°, 38.72°, 48.81°, 58.30°, 61.60°, 66.32°, and 68.12° are indexed to the monoclinic crystal system of CuO, referring to card #01-089-5895. The X-ray diffractogram of the Cu/NaY catalyst indicated that there were no modifications in the original crystal structure of the zeolite, probably due to the fine distribution of copper on the zeolite structure [50].

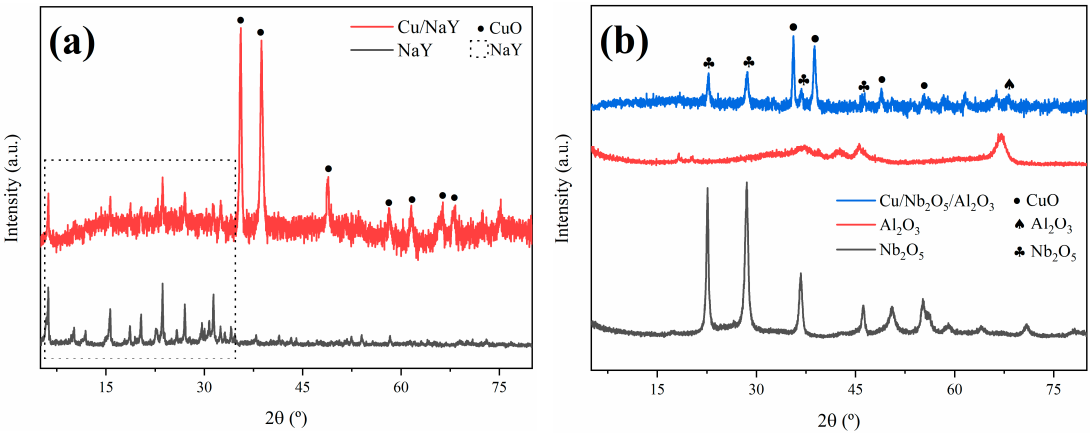

Figure 3. DRX patterns of (**a**) Cu/NaY and (**b**) $Cu/Nb_2O_5/Al_2O_3$.

The $Cu/Nb_2O_5/Al_2O_3$ catalyst presented diffraction peaks at 2θ = 35.57°, 38.72°, 48.81°, and 56.72°, which are indexed to the monoclinic crystal system of CuO in card #01-089-5895. The diffraction peak at 2θ = 67.03° is indexed to the hexagonal crystal system of Al_2O_3 in card #00-013-0373, while the diffraction peaks at 2θ = 22.60°, 28.58°, 36.71°, and 46.23° are indexed to the hexagonal crystal system of Nb_2O_5 in card #00-028-0317. Both copper oxide and niobium pentoxide are present in the diffractogram with significant intensities, indicating that the precursors maintained their defined crystal lattice even after the catalyst synthesis. Also, alumina diffraction peaks are almost imperceptible, indicating a high dispersion of alumina in niobium oxide [51].

The crystallite size has important implications for the rate of molecular diffusion and the contribution of the external surface area to adsorption and desorption rates. For the calculation of the crystallite size of the active phase in both catalysts, the (−111) diffraction peak at 2θ = 35.57° of copper oxide was considered. The result was approximately 55 nm for both catalysts, indicating that the change of support did not cause an alteration in the crystallite size of the active phase. For the calculation of the support crystallite sizes, the (533) diffraction peak at 2θ = 23.64° of NaY and the (100) diffraction peak at 2θ = 28.58° of Nb_2O_5 were considered, resulting in 114 nm and 43 nm, respectively. Kugai et al. [52] concluded that the smaller the crystallite size of the support, the greater the dispersion of the active phase and consequently the higher the catalytic activity, indicating that the catalyst performance strongly depends on the surface area and crystallite sizes.

3.1.3. Textural Parameters

The determination of the textural parameters of the synthesized materials and their precursors is relevant to understand their SRE catalytic performance. The parameters obtained through N_2 physisorption are presented in Table 2, while the N_2 adsorption/desorption isotherms are shown in Figure 4. For the Cu/NaY catalyst, the isotherm exhibits characteristics of type IV according to I.U.P.A.C. [53], which is attributed to the presence of micropores associated with mesopores. The formation of a round knee-like feature at the

beginning of the isotherm is related to the formation of adsorbed N_2 monolayers inside micropores [54], while the increase in relative pressure improves adsorption as the material mesopores are filled. For the $Cu/Nb_2O_5/Al_2O_3$ catalyst, the obtained isotherm is of type V, which is also associated with mesoporous materials with weak adsorbate–adsorbent interactions. In both isotherms, there was hysteresis in N_2 desorption, which is characteristic of capillary condensation in mesoporous materials [55]. For Cu/NaY, the hysteresis of type H4 is associated with narrow slit-like pores, while for $Cu/Nb_2O_5/Al_2O_3$, the hysteresis of type H3 refers to non-rigid aggregates of plate-like particles forming slit pores, typical of non-uniform pore sizes and shapes as observed by SEM.

Table 2. Textural parameters of the catalysts and precursors.

Sample	Surface Area ($m^2\ g^{-1}$)	Pore Volume ($cm^3\ g^{-1}$)	Micropore Volume ($cm^3\ g^{-1}$)	Pore Diameter (nm)
Nb_2O_5	71.73	0.3700	0.3200	8.24
NaY	588.49	0.1479	0.0281	1.74
Al_2O_3	99.26	0.1799	0,0389	7.24
Cu/NaY	210.40	0.1180	0.1114	2.24
$Cu/Nb_2O_5/Al_2O_3$	26.00	0.0617	0.0106	9.56

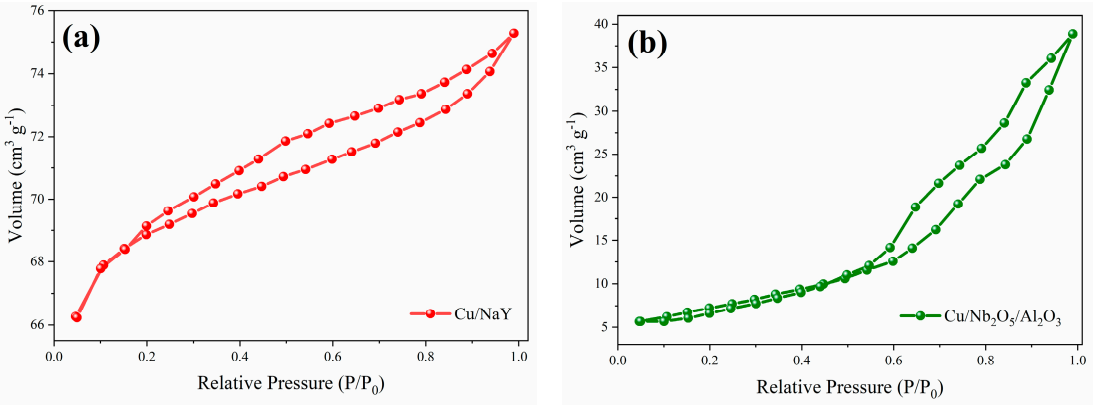

Figure 4. N_2 adsorption/desorption isotherms of the catalysts (**a**) Cu/NaY and (**b**) $Cu/Nb_2O_5/Al_2O_3$.

Concerning the obtained values for the textural parameters, the surface areas of the catalytic supports were similar to other studies involving NaY [56,57], Nb_2O_5 [11,45], and Al_2O_3 [58,59]. For the catalysts, a noticeable reduction in surface area and pore volume was observed, compared to their corresponding precursors. This effect is strongly associated with the possible obstruction of smaller pore diameters (micropores) by deposition of copper oxides inside the catalyst structure, as evidenced by the reduction in micropore volume. However, despite this reduction, a significant variation in textural properties was detected among our catalysts. This reinforces the possible influence of the support type on the catalyst performance, as it plays a fundamental role in the reaction. Cu/NaY has a significantly higher surface area than $Cu/Nb_2O_5/Al_2O_3$, which is expected to result in a superior catalytic performance of the former compared to the latter. This advantageous characteristic of Cu/NaY has been attributed to the three-dimensional pore structure of zeolite NaY [60].

The FTIR spectra of the synthesized catalysts and both Nb_2O_5 and NaY supports are shown in Figures 5a and 5b, respectively. The band at approximately 3500 cm^{-1}, observed in all spectra, reveals the presence of surface hydroxyl groups in these materials [29,61]. The main NaY vibration modes were identified as the strong band located at 1029 cm^{-1} and the lower intensity band at 469 cm^{-1}, which correspond to the internal vibrations of the tetrahedral units of the zeolite, while the bands identified at 1150, 794, and 570 cm^{-1} were attributed to the external linkages between the $(Si/Al)O_4$ tetrahedra [62]. Sensitive bands did not show significant changes in the Cu/NaY spectrum compared to those of

NaY. On the other hand, the band at 570 cm^{-1}, attributed to the polyhedral ring in the zeolite structure, showed a slight alteration that may be associated with the binding of copper. According to previous studies, copper oxide (CuO) bands are present between the wavenumbers of 610 and 500 cm^{-1} [62,63].

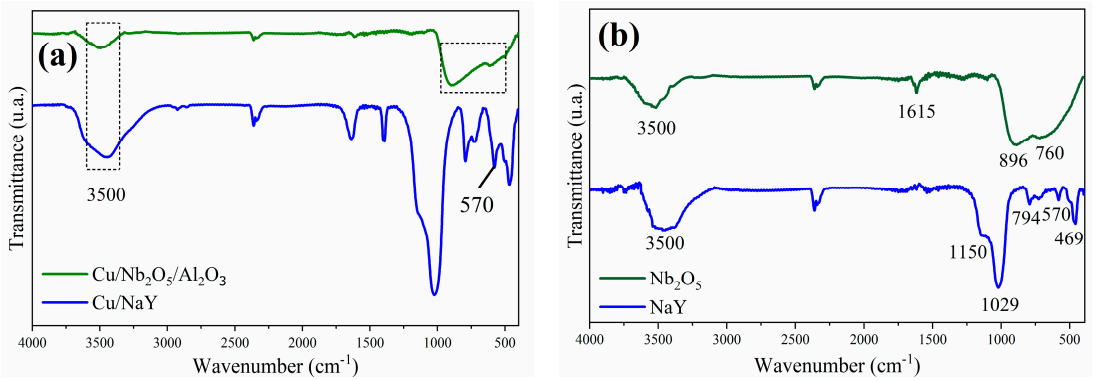

Figure 5. Infrared spectra of the catalysts (**a**) Cu/NaY and $Cu/Nb_2O_5/Al_2O_3$ and of the precursors (**b**) NaY and Nb_2O_5.

The FTIR spectrum of Nb_2O_5 (Figure 5b) shows strong and broad bands in the region between 500 and 900 cm^{-1}. The band centered at 896 cm^{-1} is attributed to the Nb-O stretching vibration and the band at 760 cm^{-1} to the Nb-O-Nb vibration [64]. The narrower band at 1622 cm^{-1} is attributed to water molecules adsorbed on the Nb_2O_5 surface [65]. The presence of niobium pentoxide was confirmed by the presence of its main vibration modes in the FTIR spectrum of the $Cu/Nb_2O_5/Al_2O_3$ catalyst (Figure 5a). Alterations were also noted in the intensity of the two bands between 500 and 900 cm^{-1}, and in the resolution between them, when compared to the Nb_2O_5 spectrum. These changes are attributed to the binding with copper, as we are once again referring to the region of copper oxide bands.

3.1.4. Temperature-Programmed Desorption (TPD)

Analyses of both catalysts by TPD-NH_3 are shown in Figure 6. The NH_3 desorption profiles for Cu/NaY and $Cu/Nb_2O_5/Al_2O_3$ were confined to the 140 °C to 460 °C and 150 °C to 620 °C temperatures ranges, respectively, showing that the support type influenced the acidity of the catalyst. The peak location and wide temperature range for Cu/NaY suggest the presence of sites of weak and intermediate acid strength. By contrast, the higher temperature range for $Cu/Nb_2O_5/Al_2O_3$ is attributable to the presence of intermediate to strong acid sites. Also, Cu/NaY had a higher concentration of acid sites compared to $Cu/Nb_2O_5/Al_2O_3$ (Table 3). In general, the higher acidity of Cu/NaY may be justified by its higher surface area.

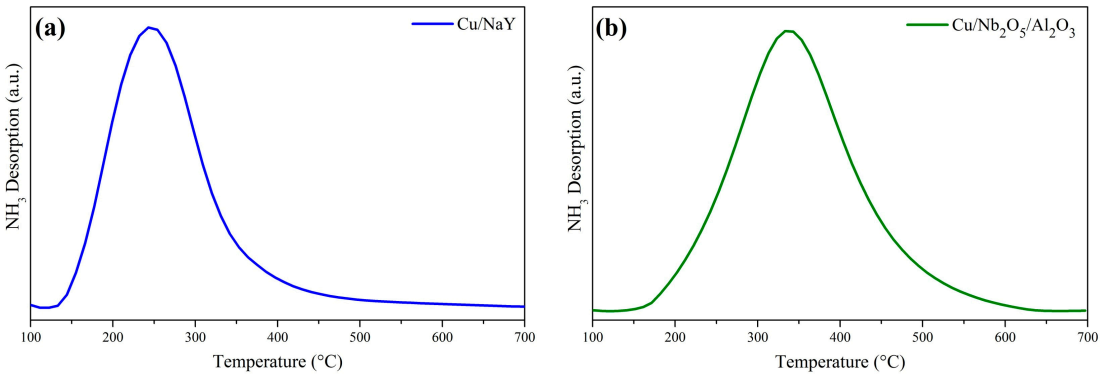

Figure 6. NH_3 desorption curves of the catalysts (**a**) Cu/NaY and (**b**) $Cu/Nb_2O_5/Al_2O_3$.

Table 3. Acidity of the synthesized catalysts by TPD-NH_3.

Sample	Chemisorbed NH_3 (mmol g^{-1})	Temperature (°C)
Cu/NaY	1.598	247
$Cu/Nb_2O_5/Al_2O_3$	0.059	336

The maximum NH_3 desorption temperature for the Cu/NaY catalyst was slightly higher than that for NaY alone, which typically ranges between 150 °C and 250 °C [66–68]. This is an indication that the incorporation of Cu into the zeolite structure increased the strength of its acid sites. On the other hand, the impregnation of Cu onto Nb_2O_5/Al_2O_3 did not have a significant influence on the desorption temperature range.

3.1.5. Temperature-Programmed Reduction (TPR)

Both catalysts displayed a wide reduction range in their TPR profiles (Figure 7). However, the position of the maximum reduction temperature of CuO for $Cu/Nb_2O_5/Al_2O_3$ was shifted to higher values compared to Cu/NaY, which may indicate a greater interaction of Cu with Nb_2O_5/Al_2O_3 compared to NaY. Reduction at temperatures below 300 °C indicated that CuO was dispersed on the catalyst surface with little interaction with the support. Above this temperature, total copper reduction was prevented in both catalytic systems by the interaction between CuO and the support surface [18,69]. Additionally, $Cu/Nb_2O_5/Al_2O_3$ showed a reduction peak with a maximum around 928 °C, which was attributed to the partial reduction of Nb_2O_5 to NbO_2 [46,70]. The hydrogen consumption of the Cu/NaY catalyst was 6.16 mmol $g_{cat}{}^{-1}$, while that of $Cu/Nb_2O_5/Al_2O_3$ was 6.38 mmol $g_{cat}{}^{-1}$—a slightly higher value due to the partial reduction of Nb_2O_5.

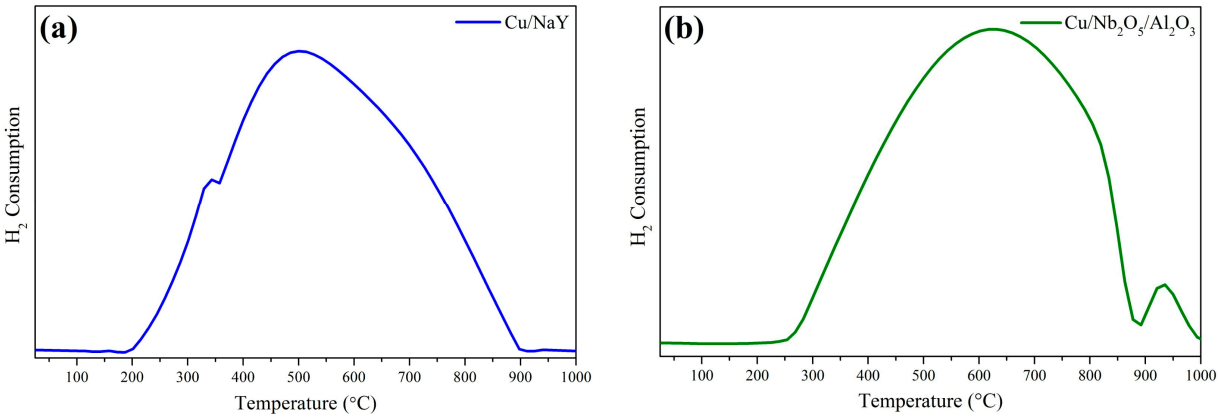

Figure 7. TPR profiles of (**a**) Cu/NaY and (**b**) $Cu/Nb_2O_5/Al_2O_3$ catalysts.

3.2. Catalytic Performance Evaluation

The main products generated with the $Cu/Nb_2O_5/Al_2O_3$ catalyst at 300 °C were hydrogen and acetaldehyde, but with a conversion below 10%. Increasing the temperature resulted in an increase in the average conversion, reaching approximately 55%, but the selectivity for hydrogen and acetaldehyde decreased while the selectivity for ethylene increased. For the Cu/NaY catalyst, a similar result was obtained at 300 °C regarding the selectivity for hydrogen and acetaldehyde, but with a higher average conversion close to 55%. Finally, with an increase in the reaction temperature to 450 °C, the conversion increased to 65% but the product distribution was greater, with CO, CO_2, CH_4, and C_2H_4 in detectable quantities.

Figure 8 shows the selectivity data for both $Cu/Nb_2O_5/Al_2O_3$ and Cu/NaY at 300 °C and 450 °C. The differences between the catalytic performances show that both support and temperature influenced the reaction efficiency. Conversion increased with increasing temperature for both catalysts, but the effect was more pronounced for the $Cu/Nb_2O_5/Al_2O_3$

catalyst. On the other hand, the selectivity for H_2 and acetaldehyde decreased with increasing temperature, and the quantity of by-products (especially ethylene) increased, with this effect being greater for the $Cu/Nb_2O_5/Al_2O_3$ catalyst.

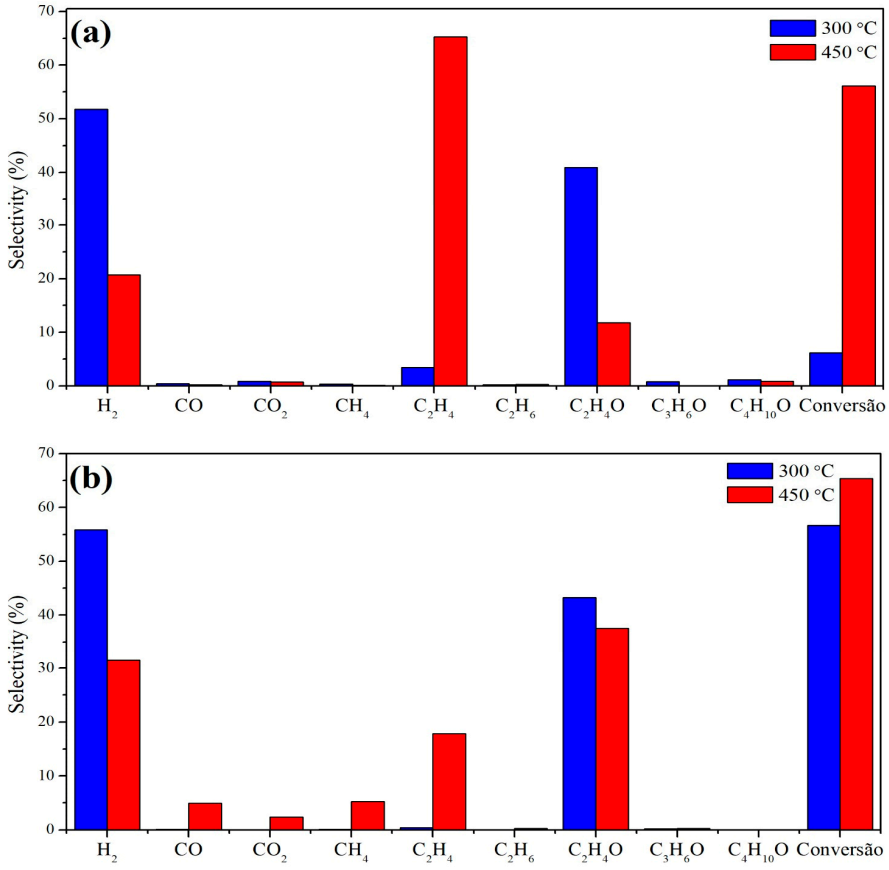

Figure 8. Average selectivity of (**a**) $Cu/Nb_2O_5/Al_2O_3$ and (**b**) Cu/NaY at 300 °C and 450 °C.

For both catalysts at 300 °C, the main reaction was ethanol dehydrogenation (Equation (5)) forming acetaldehyde and H_2, while higher temperatures favored dehydration forming ethylene (Equation (6)). Also, the use of NaY at 450 °C favored parallel reactions forming CO and CH_4 [33]. This is probably due to the presence of more pronounced acid sites in the zeolite at lower temperatures, as observed by TPD-NH_3 analysis of the Cu/NaY catalyst, where acid sites are found between 100 and 450 °C (Figure 6). Also, the high surface area of this catalyst contributed to the greater exposure of acid sites, as well as the catalytically active copper sites on the catalyst surface, promoting parallel reactions that are part of the ethanol reforming reaction pathway. This explains the detection of reaction intermediates such as acetaldehyde.

$$C_2H_5OH \rightarrow C_2H_4O + H_2 \quad (5)$$

$$C_2H_5OH \rightarrow C_2H_4 + H_2O \quad (6)$$

The selectivity of $Cu/Nb_2O_5/Al_2O_3$ to C_2H_4 was higher than that of Cu/NaY. The TPD-NH_3 of this catalyst showed acid sites of greater strength due to the desorption of NH_3 at higher temperatures, which may be connected to the higher formation of C_2H_4 [70]. Lorenzut et al. [71] observed the same low selectivity behavior for Cu catalysts supported on ZnO/Al_2O_3. Also, the support seemed to have influenced the reaction pathway, since Nb_2O_5 is an n-type semiconductor that may have driven the selectivity toward ethylene. For the $Cu/Nb_2O_5/Al_2O_3$ catalyst, the formation of CO_2 was limited at both temperatures, while for Cu/NaY, CO_2 formation was more pronounced at 450 °C, indicating the occurrence of ethanol reforming.

Both catalysts exhibited more stability at 300 °C (Figure 9) because, at 450 °C, C_2H_4 formation accelerated deactivation by coke deposition [72]. For the Cu/NaY catalyst, the carbon balance at 300 °C and 450 °C was 87% and 79%, respectively, whereas for $Cu/Nb_2O_5/Al_2O_3$, the carbon balance was 99% at 300 °C and 83% at 450 °C. In general, values below 100% may suggest the formation of coke on the catalyst surface [73]. Overall, the results highlight the strong influence of the catalytic support on the steam reforming of ethanol for H_2 production.

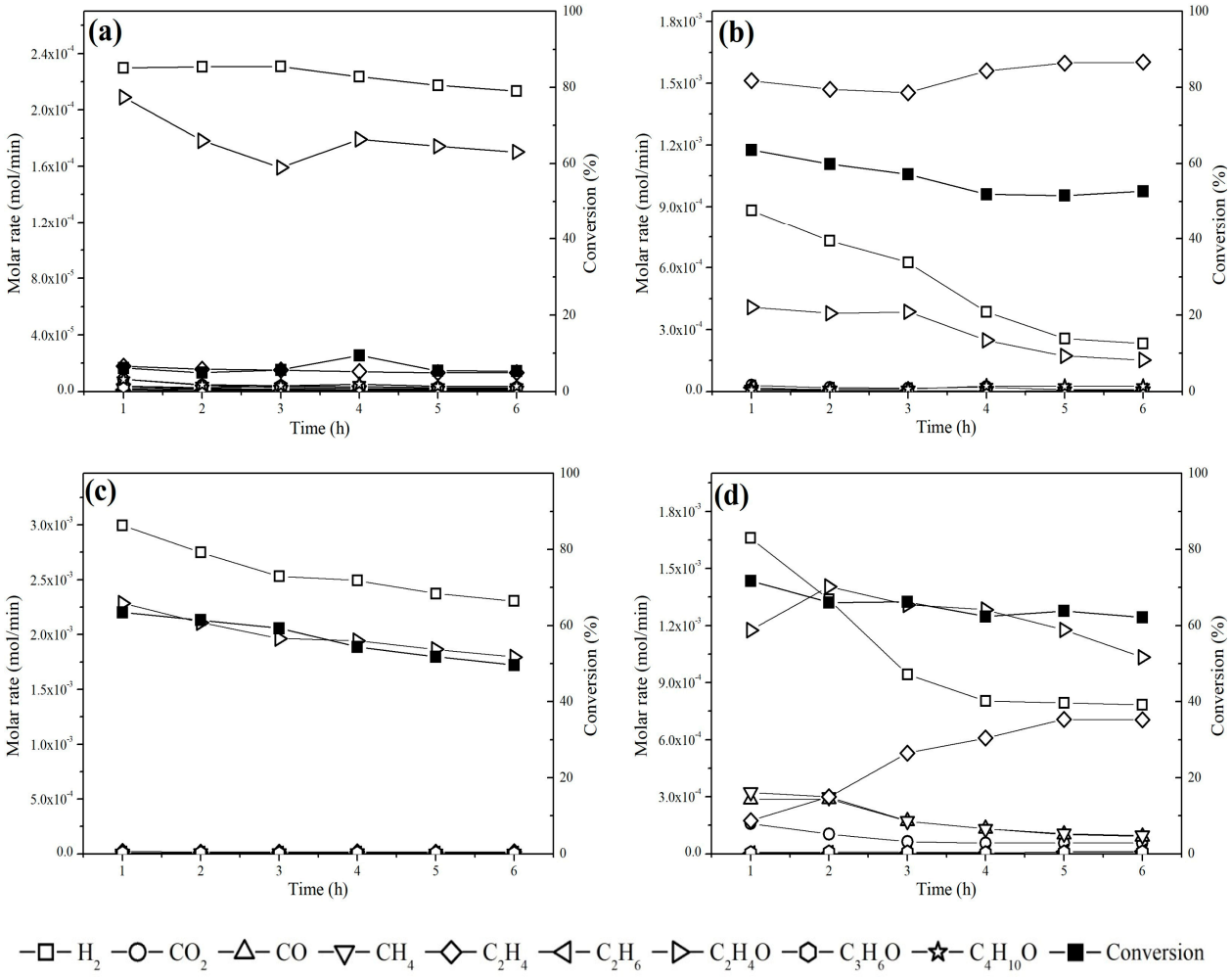

Figure 9. Molar rate as a function of time for $Cu/Nb_2O_5/Al_2O_3$ at (**a**) 300 °C and (**b**) 450 °C and Cu/NaY at (**c**) 300 °C and (**d**) 450 °C.

The Cu/NaY catalyst showed a higher ethanol conversion rate compared to $Cu/Nb_2O_5/Al_2O_3$, suggesting that support properties such as surface area, pore volume, and pore size significantly influenced the catalytic performance. The porous structure and higher surface area of NaY may have facilitated copper dispersion and interaction with the reactants, enhancing the catalytic activity. Additionally, zeolites have a structure with a regular arrangement of uniform micropores that promote greater selectivity for H_2 formation. Furthermore, the acidity measurements revealed that the incorporation of copper into NaY increases the strength of the acid sites, as indicated by the higher desorption temperature found for Cu/NaY compared to pure NaY in other studies [74–76]. This increased acidity may have contributed to the improvement of the catalytic activity by influencing the adsorption and breakdown of ethanol molecules.

The catalytic performance of Cu/SiO [77] and CuO/ZrO_2 [73] in SRE reactions was evaluated at lower temperatures, e.g., 300 °C and 350 °C. The former showed no catalytic

activity, while the latter produced hydrogen (Y = 36%), acetaldehyde (S = 58%), and acetic acid (S = 24%) as the main products, achieving a conversion of 90%. Only at 500 °C did the Cu/SiO catalyst produce acetaldehyde with a conversion of 12%. Cu/Nb_2O_5 resulted in catalytic conversions below 10% at 450 °C [18], producing 60% H_2 and 35% C_2H_4O, on average, along with co-products such as ethylene and ethyl ether (<5%). These results, along with those obtained in this work, highlight the role of the catalytic support in SRE. Therefore, a careful selection of the support is crucial for optimizing the performance of copper catalysts in H_2 production by SRE.

4. Conclusions

The steam reforming of ethanol was viable using copper-based catalysts supported on a NaY zeolite (Cu/NaY) and niobium-aluminum oxides ($Cu/Nb_2O_5/Al_2O_3$). The physicochemical properties of the two catalysts were different due to differences in the support properties. Nevertheless, copper particles were well dispersed in both catalysts, contributing to achieving better catalytic performances. Both catalysts were active in the steam reforming of ethanol, but Cu/NaY was best for H_2 production at 450 °C, with CO_2 formation remaining constant throughout the reaction course. Therefore, this catalyst has potential for large-scale operations and, with the addition of a small amount of acidity dopants, it may become even more selective for H_2 production by ethanol reforming. Finally, the support effect was demonstrated as a relevant parameter for optimal SRE catalytic performance. The greatest limitation of this work was catalyst shortage, and this leads to the emergence of synthesizing larger quantities of the most efficient NaY-supported copper catalyst for further optimization studies including the addition of acidity dopants to enhance the selectivity for hydrogen production. Additionally, studies on catalyst recovery and reuse must be performed, as well as a detailed economic analysis for process development on an industrial scale.

Author Contributions: Conceptualization, R.C.P.R.-D., L.P.R. and M.d.S.; methodology, R.C.P.R.-D., A.D.G. and B.R.F.; investigation, A.D.G. and B.R.F.; resources, L.P.R., M.d.S. and R.C.P.R.-D.; data curation, R.P.N., P.D.M., A.D.G. and B.R.F.; writing—original draft preparation, P.D.M., R.P.N., R.C.P.R.-D. and A.D.G.; writing—review and editing, P.D.M., R.P.N., A.D.G., L.P.R. and R.C.P.R.-D.; supervision, R.C.P.R.-D. and L.P.R.; funding acquisition, L.P.R. All authors have read and agreed to the published version of the manuscript.

Funding: The authors are grateful for the financial support of Conselho Nacional de Desenvolvimento Científico e Tecnológico (CNPq, Brazil—grant number 315930/2021-7), Fundação Araucária (grant agreement 002/2021, process #17.521.887-4—NAPI-HCR project), and Coordenação de Aperfeiçoamento de Pessoal de Nível Superior (CAPES, Brazil—Finance Code 001).

Data Availability Statement: The original contributions presented in the study are included in the article. Further inquiries can be directed to the corresponding author.

Acknowledgments: The support of the Multi-User Laboratories for Materials Characterization (CMCM) and Chemical Analysis (LAMAQ) at the Federal Technological University of Paraná (UTFPR), the Department of Soils at the Agrarian Sciences Campus of the Federal University of Paraná (UFPR), the Companhia Brasileira de Metalurgia e Mineração (CBMM, Minas Gerais, Brazil), and the Catalysis Laboratory (LabCat) at the State University of Maringá (UEM) are greatly acknowledged.

Conflicts of Interest: The authors declare no conflicts of interest.

References

1. Luo, M.; Li, S.; Di, Z.; Yang, Z.; Chou, W.; Shi, B. Fischer-Tropsch Synthesis: Effect of Nitric Acid Pretreatment on Graphene-Supported Cobalt Catalyst. *Appl. Catal. A Gen.* **2020**, *599*, 117608. [CrossRef]
2. Yousefian, F.; Babatabar, M.A.; Eshaghi, M.; Poor, S.M.; Tavasoli, A. Pyrolysis of Rice Husk, Coconut Shell, and Cladophora Glomerata Algae and Application of the Produced Biochars as Support for Cobalt Catalyst in Fischer–Tropsch Synthesis. *Fuel Process. Technol.* **2023**, *247*, 107818. [CrossRef]
3. Liu, Y.; Zou, R.; Qin, B.; Gan, J.; Peng, X. Energy-Efficient Monosaccharides Electrooxidation Coupled with Green Hydrogen Production by Bifunctional Co_9S_8/Ni_3S_2 Electrode. *Chem. Eng. J.* **2022**, *446*, 136950. [CrossRef]

4. Mert, M.E.; Edis, C.; Akyıldız, Ş.; Demir, B.N.; Nazligul, H.; Gurdal, Y.; Doğru Mert, B. Design and Performance Analysis of a PV-Assisted Alkaline Electrolysis for Hydrogen Production: An Experimental and Theoretical Study. *Fuel* **2024**, *355*, 129497. [CrossRef]
5. Vadalà, M.; Kröll, E.; Küppers, M.; Lupascu, D.C.; Brunstermann, R. Hydrogen Production via Dark Fermentation by Bacteria Colonies on Porous PDMS-Scaffolds. *Int. J. Hydrogen Energy* **2023**, *48*, 25274–25284. [CrossRef]
6. Öztan, H.; Çapoğlu, İ.K.; Uysal, D.; Doğan, Ö.M. A Parametric Study to Optimize the Temperature of Hazelnut and Walnut Shell Gasification for Hydrogen and Methane Production. *Bioresour. Technol. Rep.* **2023**, *23*, 101581. [CrossRef]
7. Guan, D.; Wang, F.; Zhang, X.; Dou, W.; Sun, Y. Comprehensive Study on Catalytic Coating Tubular Reactor with Electromagnetic Induction Heating for Hydrogen Production through Methanol Steam Reforming. *Int. J. Hydrogen Energy* **2024**, *50*, 1–17. [CrossRef]
8. Hu, Y.; He, W.; Shen, Y. Recyclable NiMnOx/NaF Catalysts: Hydrogen Generation via Steam Reforming of Formaldehyde. *Fuel* **2023**, *354*, 129311. [CrossRef]
9. Zoppi, G.; Pipitone, G.; Gruber, H.; Weber, G.; Reichhold, A.; Pirone, R.; Bensaid, S. Aqueous Phase Reforming of Pilot-Scale Fischer-Tropsch Water Effluent for Sustainable Hydrogen Production. *Catal. Today* **2021**, *367*, 239–247. [CrossRef]
10. Levikhin, A.A.; Boryaev, A.A. High-Temperature Reactor for Hydrogen Production by Partial Oxidation of Hydrocarbons. *Int. J. Hydrogen Energy* **2023**, *48*, 28187–28204. [CrossRef]
11. da Silva, F.A.; Dancini-Pontes, I.; DeSouza, M.; Fernandes, N.R.C. Kinetics of Ethanol Steam Reforming over Cu–Ni/NbxOy Catalyst. *React. Kinet. Mech. Catal.* **2017**, *122*, 557–574. [CrossRef]
12. Shtyka, O.; Dimitrova, Z.; Ciesielski, R.; Kedziora, A.; Mitukiewicz, G.; Leyko, J.; Maniukewicz, W.; Czylkowska, A.; Maniecki, T. Steam Reforming of Ethanol for Hydrogen Production: Influence of Catalyst Composition (Ni/Al_2O_3, Ni/Al_2O_3–CeO_2, Ni/Al_2O_3–ZnO) and Process Conditions. *React. Kinet. Mech. Catal.* **2021**, *132*, 907–919. [CrossRef]
13. Haryanto, A.; Fernando, S.; Murali, N.; Adhikari, S. Current Status of Hydrogen Production Techniques by Steam Reforming of Ethanol: A Review. *Energy Fuels* **2005**, *19*, 2098–2106. [CrossRef]
14. Zanchet, D.; Santos, J.B.O.; Damyanova, S.; Gallo, J.M.R.; Bueno, J.M.C. Toward Understanding Metal-Catalyzed Ethanol Reforming. *ACS Catal.* **2015**, *5*, 3841–3863. [CrossRef]
15. Trane-Restrup, R.; Dahl, S.; Jensen, A.D. Steam Reforming of Ethanol: Effects of Support and Additives on Ni-Based Catalysts. *Int. J. Hydrogen Energy* **2013**, *38*, 15105–15118. [CrossRef]
16. Wurzler, G.T.; Rabelo-Neto, R.C.; Mattos, L.V.; Fraga, M.A.; Noronha, F.B. Steam Reforming of Ethanol for Hydrogen Production over MgO—Supported Ni-Based Catalysts. *Appl. Catal. A Gen.* **2016**, *518*, 115–128. [CrossRef]
17. Palma, V.; Ruocco, C.; Castaldo, F.; Ricca, A.; Boettge, D. Ethanol Steam Reforming over Bimetallic Coated Ceramic Foams: Effect of Reactor Configuration and Catalytic Support. *Int. J. Hydrogen Energy* **2015**, *40*, 12650–12662. [CrossRef]
18. Alonso, C.G.; Furtado, A.C.; Cantão, M.P.; Andreo dos Santos, O.A.; Camargo Fernandes-Machado, N.R. Reactions over Cu/Nb_2O_5 Catalysts Promoted with Pd and Ru during Hydrogen Production from Ethanol. *Int. J. Hydrogen Energy* **2009**, *34*, 3333–3341. [CrossRef]
19. Chen, F.; Tao, Y.; Ling, H.; Zhou, C.; Liu, Z.; Huang, J.; Yu, A. Ni-Cu Bimetallic Catalysts on Yttria-Stabilized Zirconia for Hydrogen Production from Ethanol Steam Reforming. *Fuel* **2020**, *280*, 118612. [CrossRef]
20. Ranjekar, A.M.; Yadav, G.D. Steam Reforming of Ethanol for Hydrogen Production: Efficacy of Ceria Promoted Cu–Co on Mesoporous Cellular Foam Silica. *Int. J. Hydrogen Energy* **2023**, *48*, 31550–31570. [CrossRef]
21. Guarido, C.E.M.; Cesar, D.V.; Souza, M.M.V.M.; Schmal, M. Ethanol Reforming and Partial Oxidation with Cu/Nb_2O_5 Catalyst. *Catal. Today* **2009**, *142*, 252–257. [CrossRef]
22. Hou, T.; Zhang, S.; Chen, Y.; Wang, D.; Cai, W. Hydrogen Production from Ethanol Reforming: Catalysts and Reaction Mechanism. *Renew. Sustain. Energy Rev.* **2015**, *44*, 132–148. [CrossRef]
23. Mariño, F.J.; Cerrella, E.G.; Duhalde, S.; Jobbagy, M.; Laborde, M.A. Hydrogen from Steam Reforming of Ethanol. Characterization and Performance of Copper-Nickel Supported Catalysts. *Int. J. Hydrogen Energy* **1998**, *23*, 1095–1101. [CrossRef]
24. Ni, M.; Leung, D.Y.C.; Leung, M.K.H. A Review on Reforming Bio-Ethanol for Hydrogen Production. *Int. J. Hydrogen Energy* **2007**, *32*, 3238–3247. [CrossRef]
25. Snytnikov, P.V.; Badmaev, S.D.; Volkova, G.G.; Potemkin, D.I.; Zyryanova, M.M.; Belyaev, V.D.; Sobyanin, V.A. Catalysts for Hydrogen Production in a Multifuel Processor by Methanol, Dimethyl Ether and Bioethanol Steam Reforming for Fuel Cell Applications. *Int. J. Hydrogen Energy* **2012**, *37*, 16388–16396. [CrossRef]
26. Furtado, A.C.; Alonso, C.G.; Cantão, M.P.; Fernandes-Machado, N.R.C. Bimetallic Catalysts Performance during Ethanol Steam Reforming: Influence of Support Materials. *Int. J. Hydrogen Energy* **2009**, *34*, 7189–7196. [CrossRef]
27. Denis, A.; Grzegorczyk, W.; Gac, W.; Machocki, A. Steam Reforming of Ethanol over Ni/Support Catalysts for Generation of Hydrogen for Fuel Cell Applications. *Catal. Today* **2008**, *137*, 453–459. [CrossRef]
28. Inokawa, H.; Nishimoto, S.; Kameshima, Y.; Miyake, M. Difference in the Catalytic Activity of Transition Metals and Their Cations Loaded in Zeolite Y for Ethanol Steam Reforming. *Int. J. Hydrogen Energy* **2010**, *35*, 11719–11724. [CrossRef]
29. Nippes, R.P.; Frederichi, D.; Olsen Scaliante, E.M.H.N. Enhanced Photocatalytic Performance under Solar Radiation of ZnO through Hetero-Junction with Iron Functionalized Zeolite. *J. Photochem. Photobiol. A Chem.* **2021**, *418*, 113373. [CrossRef]
30. Mohamed, R.M.; Mkhalid, I.A.; Barakat, M.A. Rice Husk Ash as a Renewable Source for the Production of Zeolite NaY and Its Characterization. *Arab. J. Chem.* **2015**, *8*, 48–53. [CrossRef]

31. Tolentino, C.M.C.; de Luna, M.D.G.; Futalan, C.M.; Choi, A.E.S.; Manegdeg, F.G.; Grisdanurak, N. Influence of Hydrocarbons on Hydrogen Chloride Removal from Refinery Off-Gas by Zeolite NaY Derived from Rice Husks. *Sci. Total Environ.* **2020**, *728*, 138782. [CrossRef] [PubMed]
32. Ali, M.M.M.; Ahmed, M.J.; Hameed, B.H. NaY Zeolite from Wheat (*Triticum aestivum* L.) Straw Ash Used for the Adsorption of Tetracycline. *J. Clean. Prod.* **2018**, *172*, 602–608. [CrossRef]
33. Campos-Skrobot, F.C.; Rizzo-Domingues, R.C.P.; Fernandes-Machado, N.R.C.; Cantão, M.P. Novel Zeolite-Supported Rhodium Catalysts for Ethanol Steam Reforming. *J. Power Sources* **2008**, *183*, 713–716. [CrossRef]
34. Kwak, B.S.; Lee, J.S.; Lee, J.S.; Choi, B.-H.; Ji, M.J.; Kang, M. Hydrogen-Rich Gas Production from Ethanol Steam Reforming over Ni/Ga/Mg/Zeolite Y Catalysts at Mild Temperature. *Appl. Energy* **2011**, *88*, 4366–4375. [CrossRef]
35. Lee, J.-S.; Kim, J.-E.; Kang, M.-S. Hydrogen Production from Ethanol Steam Reforming over SnO_2-K_2O/Zeolite Y Catalyst. *Bull. Korean Chem. Soc.* **2011**, *32*, 1912–1920. [CrossRef]
36. Androulakis, A.; Yentekakis, I.V.; Panagiotopoulou, P. Dry Reforming of Methane over Supported Rh and Ru Catalysts: Effect of the Support (Al_2O_3, TiO_2, ZrO_2, YSZ) on the Activity and Reaction Pathway. *Int. J. Hydrogen Energy* **2023**, *48*, 33886–33902. [CrossRef]
37. Kharaji, A.G.; Shariati, A.; Takassi, M.A. A Novel γ-Alumina Supported Fe-Mo Bimetallic Catalyst for Reverse Water Gas Shift Reaction. *Chin. J. Chem. Eng.* **2013**, *21*, 1007–1014. [CrossRef]
38. Pastor-Pérez, L.; Shah, M.; le Saché, E.; Ramirez Reina, T. Improving Fe/Al2O3 Catalysts for the Reverse Water-Gas Shift Reaction: On the Effect of Cs as Activity/Selectivity Promoter. *Catalysts* **2018**, *8*, 608. [CrossRef]
39. Ranjbar, A.; Aghamiri, S.F.; Irankhah, A. Effect of MgO/Al_2O_3 Ratio in the Support of Mesoporous Ni/MgO–Al_2O_3 Catalysts for CO_2 Utilization via Reverse Water Gas Shift Reaction. *Int. J. Hydrogen Energy* **2023**, *48*, 19115–19125. [CrossRef]
40. Xiao, T.; Xie, J.; Cheng, J.; Dai, X.; Lu, S.; Zuo, R.; Li, Z.; Yang, Z. Al_2O_3 Supported NiCu Alloy as a Stable Catalyst for Selective Hydrogenation of Phthalic Anhydride to Phthalide. *Appl. Catal. A Gen.* **2023**, *660*, 119189. [CrossRef]
41. Yao, X.; Gao, F.; Dong, L. The Application of Incorporation Model in γ-Al_2O_3 Supported Single and Dual Metal Oxide Catalysts: A Review. *Chin. J. Catal.* **2013**, *34*, 1975–1985. [CrossRef]
42. Ji, N.; Yin, J.; Rong, Y.; Li, H.; Yu, Z.; Lei, Y.; Wang, S.; Diao, X. More than a Support: The Unique Role of Nb_2O_5 in Supported Metal Catalysts for Lignin Hydrodeoxygenation. *Catal. Sci. Technol.* **2022**, *12*, 3751–3766. [CrossRef]
43. Zhang, C.; Wu, J.; Hua, C.; Zhu, L.; Qiu, K.; Wang, S. Hydrodeoxygenation Performance of Lignin-Derived Phenolics to Cycloalkanes: Insights into the Crystal Structures of the Nb_2O_5 Support. *Energy Fuels* **2023**, *37*, 14006–14020. [CrossRef]
44. Nippes, R.P.; Gomes, A.D.; Macruz, P.D.; de Souza, M. Photocatalytic Removal of 17β-Estradiol from Water Using a Novel Bimetallic NiCu/Nb_2O_5 Catalyst. *Environ. Sci. Pollut. Res.* **2023**, *30*, 103731–103742. [CrossRef] [PubMed]
45. Nippes, R.P.; Macruz, P.D.; Gomes, A.D.; Girotto, C.P.; Scaliante, M.H.N.O.; de Souza, M. Removal of Reactive Blue 250 Dye from Aqueous Medium Using Cu/Fe Catalyst Supported on Nb2O5 through Oxidation with H_2O_2. *React. Kinet. Mech. Catal.* **2022**, *135*, 2697–2717. [CrossRef]
46. Dancini-Pontes, I.; DeSouza, M.; Silva, F.A.; Scaliante, M.H.N.O.; Alonso, C.G.; Bianchi, G.S.; Medina Neto, A.; Pereira, G.M.; Fernandes-Machado, N.R.C. Influence of the CeO_2 and Nb_2O_5 Supports and the Inert Gas in Ethanol Steam Reforming for H2 Production. *Chem. Eng. J.* **2015**, *273*, 66–74. [CrossRef]
47. Menezes, J.P.D.S.Q.; Manfro, R.L.; Souza, M.M.V.M. Hydrogen Production from Glycerol Steam Reforming over Nickel Catalysts Supported on Alumina and Niobia: Deactivation Process, Effect of Reaction Conditions and Kinetic Modeling. *Int. J. Hydrogen Energy* **2018**, *43*, 15064–15082. [CrossRef]
48. Pelissari Rizzo-Domingues, B.; Carolina, R.; Cantão, P.; Fernandes Machado, C.; Regina, N. Estudo de Catalisadores a Base de Cobre e Nióbia Na Reação de Reforma a Vapor de Etanol. *Acta Sci. Technol.* **2007**, *29*, 1–7. [CrossRef]
49. Trimm, D.L. *Design of Industrial Catalysts*; Elsevier Scientific Publishing Company: Amsterdam, The Netherlands, 1980; Volume 11, ISBN 0444419063.
50. Mortezaei, Z.; Zendehdel, M.; Bodaghifard, M.A. Cu Complex Grafted on the Porous Materials: Synthesis, Characterization and Comparison of Their Antibacterial Activity with Nano-Cu/NaY Zeolite. *J. Iran. Chem. Soc.* **2020**, *17*, 283–295. [CrossRef]
51. Gonçalves, J.F.; Souza, M.M.V.M. Ni/X%Nb_2O_5/Al_2O_3 Catalysts Prepared via Coprecipitation-Wet Impregnation Method for Methane Steam Reforming. *Curr. Catal.* **2020**, *9*, 80–89. [CrossRef]
52. Kugai, J.; Subramani, V.; Song, C.; Engelhard, M.; Chin, Y. Effects of Nanocrystalline CeO2 Supports on the Properties and Performance of Ni–Rh Bimetallic Catalyst for Oxidative Steam Reforming of Ethanol. *J. Catal.* **2006**, *238*, 430–440. [CrossRef]
53. Thommes, M.; Kaneko, K.; Neimark, A.V.; Olivier, J.P.; Rodriguez-Reinoso, F.; Rouquerol, J.; Sing, K.S.W. Physisorption of Gases, with Special Reference to the Evaluation of Surface Area and Pore Size Distribution (IUPAC Technical Report). *Pure Appl. Chem.* **2015**, *87*, 1051–1069. [CrossRef]
54. Beltrame, K.K.; Cazetta, A.L.; de Souza, P.S.C.; Spessato, L.; Silva, T.L.; Almeida, V.C. Adsorption of Caffeine on Mesoporous Activated Carbon Fibers Prepared from Pineapple Plant Leaves. *Ecotoxicol. Environ. Saf.* **2018**, *147*, 64–71. [CrossRef] [PubMed]
55. Zhang, H.; Liu, X.; He, G.; Zhang, X.; Bao, S.; Hu, W. Bioinspired Synthesis of Nitrogen/Sulfur Co-Doped Graphene as an Efficient Electrocatalyst for Oxygen Reduction Reaction. *J. Power Sources* **2015**, *279*, 252–258. [CrossRef]
56. Patdhanagul, N.; Srithanratana, T.; Rangsriwatananon, K.; Hengrasmee, S. Ethylene Adsorption on Cationic Surfactant Modified Zeolite NaY. *Microporous Mesoporous Mater.* **2010**, *131*, 97–102. [CrossRef]

57. Zeng, Y.; Walker, H.; Zhu, Q. Reduction of Nitrate by NaY Zeolite Supported Fe, Cu/Fe and Mn/Fe Nanoparticles. *J. Hazard. Mater.* **2017**, *324*, 605–616. [CrossRef] [PubMed]
58. Chang, H.-Y.; Lai, G.-H.; Tsai, D.-H. Aerosol Route Synthesis of Ni-CeO_2-Al_2O_3 Hybrid Nanoparticle Cluster for Catalysis of Reductive Amination of Polypropylene Glycol. *Adv. Powder Technol.* **2019**, *30*, 2293–2298. [CrossRef]
59. Fawaz, A.; Bizreh, Y.W.; Al-Hamoud, L. (NiO, Ag /Fe_2O_3-Al_2O_3-Bentonite) as Promising Catalyst for CO and HC Removal from Single-Cylinder Engine Exhaust Emissions. *Catal. Commun.* **2022**, *171*, 106521. [CrossRef]
60. Morales-Pacheco, P.; Alvarez, F.; Bucio, L.; Domínguez, J.M. Synthesis and Structural Properties of Zeolitic Nanocrystals II: FAU-Type Zeolites. *J. Phys. Chem. C* **2009**, *113*, 2247–2255. [CrossRef]
61. Ameri, A.; Faramarzi, M.A.; Tarighi, S.; Shakibaie, M.; Ameri, A.; Ramezani-Sarbandi, A.; Forootanfar, H. Removal of Dyes by Trametes Versicolor Laccase Immobilized on NaY-Zeolite. *Chem. Eng. Res. Des.* **2023**, *197*, 240–253. [CrossRef]
62. El-Bahy, Z.M. Oxidation of Carbon Monoxide over Cu- and Ag-NaY Catalysts with Aqueous Hydrogen Peroxide. *Mater. Res. Bull.* **2007**, *42*, 2170–2183. [CrossRef]
63. Xu, Y.; Chen, D.; Jiao, X. Fabrication of CuO Pricky Microspheres with Tunable Size by a Simple Solution Route. *J. Phys. Chem. B* **2005**, *109*, 13561–13566. [CrossRef]
64. Khan, I.; Baig, N.; Qurashi, A. Graphitic Carbon Nitride Impregnated Niobium Oxide (g-C_3N_4/Nb_2O_5) Type (II) Heterojunctions and Its Synergetic Solar-Driven Hydrogen Generation. *ACS Appl. Energy Mater.* **2019**, *2*, 607–615. [CrossRef]
65. da Conceição, L.R.V.; Carneiro, L.M.; Rivaldi, J.D.; de Castro, H.F. Solid Acid as Catalyst for Biodiesel Production via Simultaneous Esterification and Transesterification of Macaw Palm Oil. *Ind. Crops Prod.* **2016**, *89*, 416–424. [CrossRef]
66. Fan, D.; Jiang, S.; Qiao, K.; Zhang, S.; Wang, H.; Bo, D.; Zhang, Y.; Yu, T.; Zhai, D.; Ren, G.; et al. Cuprous Species Distribution over CuCl/NaY Dependent on Acidity and Their CO Adsorption/Desorption Performance Study. *Chem. Eng. J.* **2022**, *433*, 133763. [CrossRef]
67. Padró, C.L.; Rey, E.A.; González Peña, L.F.; Apesteguía, C.R. Activity, Selectivity and Stability of Zn-Exchanged NaY and ZSM5 Zeolites for the Synthesis of o-Hydroxyacetophenone by Phenol Acylation. *Microporous Mesoporous Mater.* **2011**, *143*, 236–242. [CrossRef]
68. Wang, Z.; Ma, R.; Song, W. Influence of HSAPO-34, HZSM-5, and NaY on Pyrolysis of Corn Straw Fermentation Residue via Py-GC/MS. *J. Anal. Appl. Pyrolysis* **2016**, *122*, 183–190. [CrossRef]
69. Ungureanu, A.; Dragoi, B.; Chirieac, A.; Ciotonea, C.; Royer, S.; Duprez, D.; Mamede, A.S.; Dumitriu, E. Composition-Dependent Morphostructural Properties of Ni–Cu Oxide Nanoparticles Confined within the Channels of Ordered Mesoporous SBA-15 Silica. *ACS Appl. Mater. Interfaces* **2013**, *5*, 3010–3025. [CrossRef] [PubMed]
70. da Silva, F.A.; Pontes, I.D.; Wurzler, G.T.; Alonso, C.G.; Neto, A.M.; Scaliante, M.H.N.O.; Desouza, M.; Fernandes-Machado, N.R.C. Production of Hydrogen from Bioethanol in Cu-Ni/NbxOy Catalysts Obtained by Different Preparation Methods. *Int. J. Hydrogen Energy* **2016**, *41*, 8111–8119. [CrossRef]
71. Lorenzut, B.; Montini, T.; De Rogatis, L.; Canton, P.; Benedetti, A.; Fornasiero, P. Hydrogen Production through Alcohol Steam Reforming on Cu/ZnO-Based Catalysts. *Appl. Catal. B* **2011**, *101*, 397–408. [CrossRef]
72. Mattos, L.V.; Jacobs, G.; Davis, B.H.; Noronha, F.B. Production of Hydrogen from Ethanol: Review of Reaction Mechanism and Catalyst Deactivation. *Chem. Rev.* **2012**, *112*, 4094–4123. [CrossRef] [PubMed]
73. Śliwa, M.; Samson, K. Steam Reforming of Ethanol over Copper-Zirconia Based Catalysts Doped with Mn, Ni, Ga. *Int. J. Hydrogen Energy* **2021**, *46*, 555–564. [CrossRef]
74. Tang, S.; Li, F.; Liu, J.; Guo, B.; Tian, Z.; Lv, J. MgO/NaY as Modified Mesoporous Catalyst for Methanolysis of Polyethylene Terephthalate Wastes. *J. Environ. Chem. Eng.* **2022**, *10*, 107927. [CrossRef]
75. Boonyoung, P.; Thongratkaew, S.; Rungtaweevoranit, B.; Pengsawang, A.; Praserthdam, P.; Sanpitakseree, C.; Faungnawakij, K. Formic Acid as a Sacrificial Agent for Byproduct Suppression in Glucose Dehydration to 5-Hydroxymethylfurfural Using NaY Zeolite Catalyst. *Bioresour. Technol.* **2024**, *392*, 130010. [CrossRef]
76. Nagpure, A.S.; Mohture, V.M.; Kayarkar, A. Green Synthesis of Highly Dispersed Cu Metal Nanoparticles Catalysts. *Inorg. Chem. Commun.* **2022**, *146*, 110118. [CrossRef]
77. Rossetti, I.; Lasso, J.; Nichele, V.; Signoretto, M.; Finocchio, E.; Ramis, G.; Di Michele, A. Silica and Zirconia Supported Catalysts for the Low-Temperature Ethanol Steam Reforming. *Appl. Catal. B* **2014**, *150–151*, 257–267. [CrossRef]